Electronic and Optical Properties of Graphene Quantum Dots: The Role of Many-Body Effects

Electronic and Optical Properties of Graphene Quantum Dots: The Role of Many-Body Effects

Yunhai Li, Huabing Shu, Shudong Wang, and Jinlan Wang*

Department of Physics, Southeast University, Nanjing, 211189, China

ⓢ Supporting Information

ABSTRACT: The electronic structure and optical properties of hexagonal armchair and zigzag-edged graphene quantum dots (GQDs) are investigated within the framework of many-body perturbation theory. Many-body effects are significant due to quantum confinement and reduced screening. The quasi-particle corrections and exciton binding energies can be several eV, much larger than those of other carbon allotropes with higher dimensionality. All the GQDs show similar absorption spectra when electron−hole interaction is included, with a prominent peak emerging below the absorption onset of the noninteracting spectrum. This peak is contributed by a pair of double-degenerate excited states originating from the transitions between degenerate frontier orbitals. The spin singlet−triplet splitting is closely related to the electron−hole overlap, which can be approximately measured by the overlap between frontier orbitals involved in the optical transitions. The strong many-body effects in GQDs should be of great importance in optoelectronic applications.
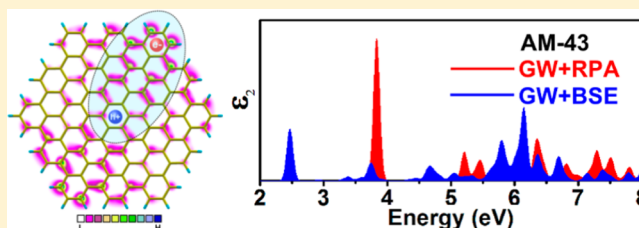
I. INTRODUCTION

Graphene, a single layer of carbon atoms arranged in a two-dimensional honeycomb lattice, was first successfully fabricated in 2004.[1] Owing to the exotic properties, such as massless carrier behavior,[2] high carrier mobility at room temperature,[3] superior thermal conductivity,[4] extremely high modulus and tensile strength,[5] and high transparency to incident light over a large wavelength range,[6] graphene has attracted enormous research interest[7] and exhibited great potential applications in electronics[8] and optoelectronics.[9] However, the gapless nature of graphene limits its applications. Many approaches, such as chemical functionalization[10] and nanopatterning,[11,12] have been employed to introduce a finite band gap into graphene. Among the methods of nanopatterning, tailoring two-dimensional (2D) graphene into quasi-0D quantum dots is widely used. Due to quantum confinement and edge effects, graphene quantum dots (GQDs) possess finite band gaps[13−15] and exhibit strong photoluminescence.[16−19] Moreover, they are superior in chemical inertness, cytotoxicity, optical stability, and raw material abundance and hold great application potential in bioimaging,[20−22] disease diagnosis,[20] drug delivery,[20] electrochemical sensor,[23] catalysis,[24] and photovoltaic devices.[25]

Further applications of GQDs require a thorough knowledge of their electronic structure and optical properties. Experiments have revealed that the band gap and HOMO/LUMO energy levels of GQDs can be independently controlled by either the lateral size or chemical functionalization.[26] The photoluminescence of GQDs is closely related to the wavelength of excitation light,[27] the lateral size,[18] the attached functional groups[28] and the pH of solution.[27,28] Theoretically, tight-binding calculations have shown that the HOMO of GQD can

be affected strongly by the geometry shape, but weakly by the edge and corner terminations,[29] and the band gap can be tuned by applying external electric field.[30,31] The lowest bright spin-singlet states in GQD are 2-fold degenerate and there exist dark singlet states below the bright one,[32] as predicted by time-dependent density functional theory (TDDFT) calculations.

It is well-known that many-body effects, namely, electron−electron and electron−hole interaction, are dominant in determining the electronic structure and optical response[33−36] of low-dimensional nanostructures due to quantum confinement and reduced screening. This has been demonstrated by earlier theoretical and experimental studies on 1D silicon nanowires,[37] carbon nanotubes[35,36,38−40] and nanoribbons,[41−44] boron nitride nanotubes[45,46] and nanoribbons,[47] and 2D graphene[48−51] and hexagonal boron nitride.[52] For example, many-body effects can increase the Fermi velocity of graphene from 0.85×10^6 to 1.15×10^6 m/s and result in the asymmetric profile of the main peak of absorption spectrum, in addition to a redshift of about 600 meV.[48] The band gap of semiconducting (8,0) single-walled carbon nanotube increases from 0.60 to 1.75 eV when many-body effects are included, and the absorption spectrum is dominated by excitonic peaks, which are absent in the single-particle picture.[35] The binding energies for the first two bright excitons are 0.99 and 0.86 eV, respectively, ten times larger than those in bulk semiconductors with similar gaps.[35] Therefore, it is essential to include many-body effects to obtain an accurate description of the electronic structure and optical

properties of GQDs. A few theoretical investigations on the many-body effects in GQDs have been reported. Güçlü et al. have explored the absorption spectrum of triangular zigzag GQDs and found that the electron–electron interactions at the Hartree–Fock level could lead to a blue-shift as large as 0.51 eV, while full configuration interaction shifts the peak toward lower energy by 0.25 eV.[53] They also predicted the existence of bright degenerate singlet excitons, which originated from the transitions between the top of the valence band and the bottom of the conduction band.[54] Nevertheless, there still lacks a high level investigation like first-principles based GW + BSE method.

In this work, we systematically study the electronic and optical properties of hexagonal GQDs with different edge types and lateral sizes by employing the GW (Green's function G and screened Coulomb interaction W) + BSE (Bethe-Salpeter equation) approach. The quasi-particle corrections and exciton binding energies can be several eVs, much larger than those of other carbon allotropes with higher dimensionality. Moreover, energy gaps, exciton binding energies, and spin singlet–triplet splitting are closely related the lateral size, edge, and corner geometry of GQDs.

II. MODEL AND COMPUTATIONAL DETAILS

Two classes of GQDs, armchair-edged (AM) and zigzag-edged (ZZ), are considered in this work. Each class consists of three different sizes, as depicted in Figure 1. It should be noted that
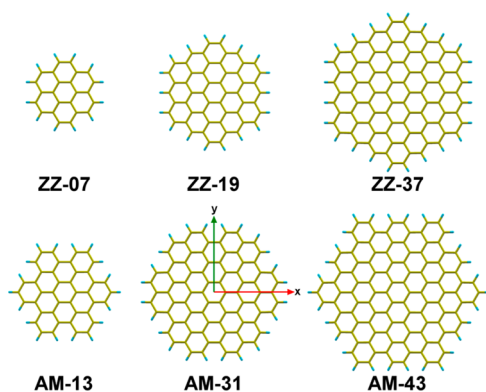
Figure 1. Structures of GQDs. Carbon and hydrogen atoms are colored in yellow and cyan, respectively. The label "AM" or "ZZ" refers to the edge type, while the following integer represents the number of aromatic rings in this GQD. The arrows on AM-31 indicate the polarization direction of incident light.

edge type and corner type are different for a given GQD.[29] Zigzag-edged GQDs have armchair corners, while armchair-edged GQDs have zigzag corners. Moreover, the corners of zigzag-edged GQDs consist of one aromatic ring, while the corners of armchair-edged ones consist of one ring (AM-13 and AM-43) or two rings (AM-31). Dangling bonds at the edge are saturated with hydrogen atoms. All the structures were fully relaxed at the DFT-LDA level without any symmetry restriction, with a criterion of total energy difference being less than 0.001 eV and forces that act on every atom being less than 0.01 eV/Å. The Perdew and Zunger[55] (PZ) functional was employed to treat the exchange-correlation of electrons. All the structures remained flat after geometry optimization, with the buckling less than 10^{-6} Å. Norm-conserving pseudopotentials and plane-wave basis set with a kinetic energy cutoff of 60 Ry were used. Periodic boundary conditions and supercell

techniques were applied, with vacuum layers in all three directions to avoid spurious interactions between periodic images. All the GQDs were positioned parallel to x–O–y plane, and the thickness of vacuum layer along the z-axis was fixed at 10 Å. The thicknesses of vacuum layers along other dimensions were determined from the convergence tests on truncation size in the following GW + BSE calculation. Only the gamma point was considered in all calculations, due to the quasi-0D nature of GQDs.

A three-step procedure[56] was employed to explore the electronic structure and optical properties of GQDs using many-body perturbation theory. First, Kohn–Sham wave functions, energies, and matrix elements of exchange-correlation operator were extracted from DFT calculations. Then the quasi-particle energies were calculated at G^0W^0 level by solving the quasi-particle equation,[57]

$$E_i^{QP} = E_i^{KS} + \langle \psi_i | \Sigma(E_i^{QP}) - V_{xc} | \psi_i \rangle \tag{1}$$

where ψ_i is the KS wave function, E_i^{KS} is the KS energy, V_{xc} is the exchange-correlation potential, and $\Sigma(E_i^{QP})$ is the frequency-dependent self-energy operator. General Plasmon-Pole approximation[57] was applied to treat the frequency dependence of self-energy operator. A total of 1440 bands were used to construct dielectric matrix and self-energy operator for ZZ-07, ZZ-19, AM-13, and AM-31, while 1200 bands were used for ZZ-37 and AM-43 considering the very expensive computational cost. The kinetic cutoffs for exchange part of self-energy operator were 60 Ry for all the GQDs, while the cutoffs for dielectric matrix and correlation part were set to the energy of the highest unoccupied orbital. The coulomb potential was truncated at the edges of Wigner-Seitz cell to simulate isolated GQDs, in both GW and the following BSE calculations.

Finally, the excitation energies and exciton wave functions were obtained by solving the Bethe–Salpeter equation (BSE),[56,58,59]

$$(E_{ck} - E_{vk})A_{vck}^S + \sum_{v'c'k'} \langle vck | K^{eh} | v'c'k' \rangle A_{v'c'k'}^S = \Omega^S A_{vck}^S \tag{2}$$

where k is the wave vector in the first Brillouin zone, E_{ck} and E_{vk} are the quasi-particle energies for the conduction and valence band states, Ω^S and A_{vck}^S are the excited eigenvalues and eigenstates, and K^{eh} is the electron–hole interaction kernel, respectively. For spin-singlet states $K^{eh} = K^d + 2K^x$, while for spin-triplet states $K^{eh} = K^d$, where K^x is the repulsive exchange term that contains bare coulomb interaction, and K^d is the direct term, which contains screened coulomb interaction and accounts for the attractive nature of electron–hole interaction. Once the excitation energies and exciton wave functions are determined, the imaginary part of dielectric function can be calculated according to the following formula:[56]

$$\varepsilon_2(\omega) = \frac{16\pi e^2}{\omega^2} \sum_S |\vec{\lambda} \cdot \langle 0 | \vec{v} | S \rangle|^2 \delta(\omega - \Omega^S) \tag{3}$$

where $\vec{\lambda}$ is the polarization vector of the incident light, $\vec{v}$ is the single-particle velocity operator and $\langle 0 | \vec{v} | S \rangle$ is the transition matrix element. To get converged absorption spectra in 0–8 eV range, 24 occupied and 60 unoccupied orbitals were used to build electron–hole interaction kernel for ZZ-07, ZZ-19, AM-13, and AM-31, while 24 and 40 orbitals for ZZ-37 and

AM-43, respectively. The kinetic cutoffs for bare interaction in exchange term and screened interaction in direct term were set to 60 Ry and the energy of the highest unoccupied orbital respectively, similar to the *GW* calculations. Also a box-shaped truncated coulomb interaction was applied, as mentioned above. Only the gamma point was involved in *GW* and BSE calculations, similar to the case of DFT.

It should be noted that the accuracy of the perturbative single-shot G^0W^0 procedure relies on the starting-point mean-field calculations.[60] In order to benchmark the dependence of the results on the exchange-correlation functional, we examined two local-density approximation (LDA) based functionals: Perdew and Zunger[55] (PZ) and Perdew and Wang[61] (PW), and two generalized gradient approximation (GGA) based functionals: Perdew, Burke, and Ernzerhof[62] (PBE) and Becke, Lee, Yang, and Parr[63,64] (BLYP). The HOMO−LUMO energy gap for GQD ZZ-07 at *GW* level obtained using these four functionals were 6.43 eV(PZ), 6.47 eV(PW), 6.19 eV(PBE), and 6.18 eV(BLYP), respectively. LDA reproduced better energy gap to the experimental value of 6.82 eV,[65] determined from gas-phase measurements, which rationalized our choice of the PZ functional.

The DFT calculations were performed using the Quantum-ESPRESSO[66] package and *GW* + BSE calculations were done using the BerkeleyGW[67] package.

III. RESULTS AND DISCUSSION

Figure 2a depicts the energy diagram of GQDs. Degeneracy of frontier orbitals is observed for all GQDs at both LDA and *GW* levels. The highest occupied molecular orbital (HOMO) and the lowest unoccupied molecular orbital (LUMO) are both double degenerate for ZZ-07, ZZ-19, ZZ-37, AM-31, and AM-43, while for AM-13, the degeneracy of LUMO is removed, which is reflected in the inconsistency between the symmetries of LUMO and LUMO+1 of AM-13, as illustrated in Figure 2b. The degeneracy of frontier orbitals is attributed to the high symmetry of hexagonal GQDs. In fact, summing the charge density for the degenerate orbitals in real space exactly yields the 6-fold rotation symmetry (Figures S1 and S2 in the Supporting Information). The degeneracy is consistent with earlier studies on hexagonal[68] and triangular[54,68] GQDs. The LDA and *GW* HOMO−LUMO energy gaps are summarized in Table 1. The *GW* energy gap of GQD ZZ-07, which is also named as coronene, is 6.43 eV, in good agreement with the experimental value 6.82 eV[65] determined from gas-phase measurements. There exists a significant increase in the gap when many-body effects are included via the *GW* approach, with the maximum being 3.53 eV for ZZ-07 and the minimum being 2.24 eV for ZZ-37. These quasi-particle corrections are much larger than those in other carbon allotropes with higher dimensionality, as 1.7 eV for diamond,[57] 1.35 and 1.04 eV for armchair-edged nanoribbon 9-AGNR (width comparable to AM-13) and 15-AGNR (width comparable to ZZ-37), respectively,[69] and 1.15 eV for single-walled nanotube (8,0)[35] are reported in previous studies, indicating the enhancement of many-body effects in GQDs due to the reduced dimensionality. The electrons in GQDs are confined within a much narrow area compared to that in other carbon allotropes of high dimensionality. Meanwhile, quantum confinement in GQDs is more prominent, which enlarges the band gap and reduces the screening as dielectric function is related to the energy difference as $\varepsilon \sim 1/\Delta E$. These two effects collaborate to enhance the interaction between electrons[45] and eventually
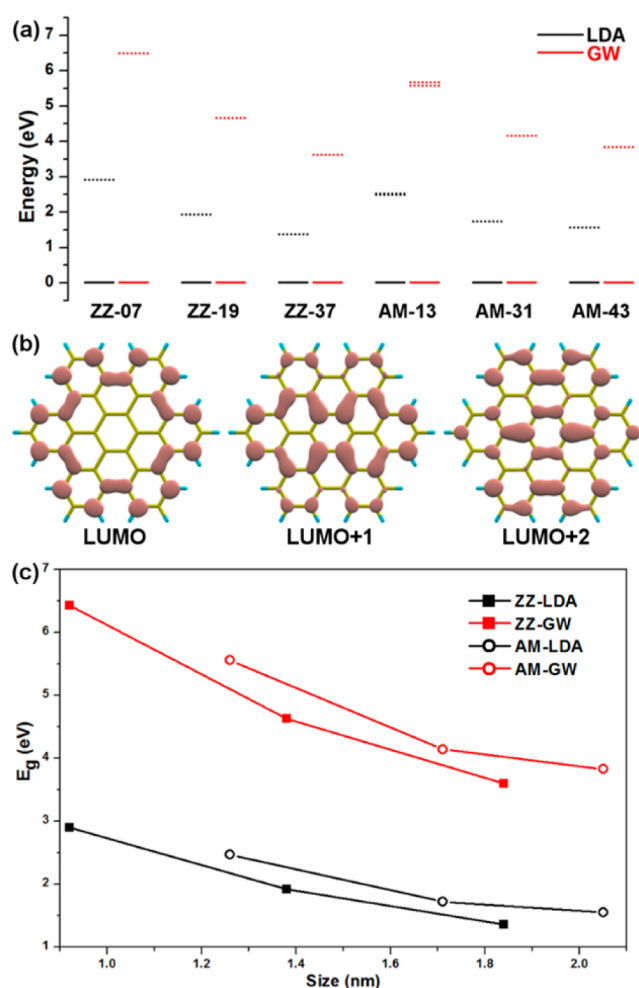
Figure 2. (a) Energy diagrams at LDA and *GW* levels. Solid and dashed line segments denote the energy levels of occupied and unoccupied orbitals, respectively. The energy levels corresponding to HOMO−1, HOMO, LUMO, and LUMO+1 are depicted for all GQDs except AM-13, for which the levels up to LUMO+2 are included. The energies of HOMO have been shifted to 0 eV for both LDA and *GW* results. Some of the levels are indistinguishable due to degeneracy and tiny energy difference. (b) Spatial distribution of the frontier orbitals of AM-13. The plotted quantity is $|\psi(r)|^2$ with the isovalue 0.001 bohr^{-3}. (c) Variation of HOMO−LUMO gap with the lateral size.

Table 1. Lateral Size, HOMO−LUMO Energy Gap at LDA and *GW* Levels, Binding Energy, Radius, and Singlet−Triplet Splitting of Bright Exciton E_x and Average Overlap of Degenerate Frontier Orbitals for All GQDs^a

| type	size	E_g-LDA	E_g-GW	E_b	radius	Δ^{S-T}	overlap
ZZ-07	0.92	2.90	6.43	2.17	0.43	1.63	0.786
ZZ-19	1.38	1.92	4.64	1.57	0.48	1.22	0.783
ZZ-37	1.84	1.36	3.60	1.24	0.57	1.00	0.781
AM-13	1.26	2.47	5.56	1.98	0.46	1.58	0.770
AM-31	1.71	1.73	4.15	1.39	0.50	0.94	0.781
AM-43	2.05	1.55	3.83	1.37	0.71	0.62	0.769

^{a}Sizes and radii are in nm and energies are in eV. The overlap is dimensionless.

result in large many-body effects in GQDs. The relation between energy gap and lateral size is depicted in Figure 2c. Both LDA and *GW* results present the same trend that the gap

decreases with the increase of the lateral size, for armchair-edged and zigzag-edged GQDs separately. This is consistent with previous DFTB results.[70] By increasing lateral size, the gap of GQD will converge to 0 eV of graphene. Moreover, armchair-edged and zigzag-edged GQDs show different convergence behaviors, as the gap of AM-43 is still larger than that of ZZ-37 (1.55 to 1.36 eV and 3.83 to 3.60 eV at LDA and *GW* levels, respectively), while the size of the former is larger than the latter (2.05−1.84 nm), reflecting the evident influence of edge geometry on the electronic structure. The different convergence behaviors of zigzag and armchair GQDs agree well with previous studies[68,71] where the energy gap of zigzag GQDs quickly decreases to zero as the size increases, while the gap of armchair ones converges much more slowly. This difference results from the edge states that localize at the middle of the edges and exist in zigzag GQDs only.[53,68] As shown in Figures S1 and S2, for zigzag GQDs, the summated charge densities for degenerate occupied and unoccupied molecular orbitals localize at the middle of the edges, while for armchair GQDs, they spread throughout the whole structure.

The absorption spectra of all GQDs at *GW* + RPA (without electron−hole interaction) and *GW* + BSE (with electron−hole interaction) levels are illustrated in Figure 3a−f, respectively.
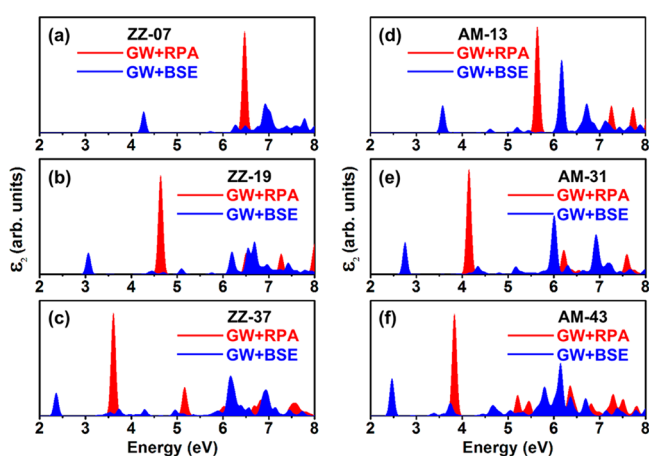
Figure 3. (a−f) Absorption spectra at *GW* + RPA (without electron−hole interaction) and *GW* + BSE (with electron−hole interaction) levels.

All spectra exhibit similar profiles when electron−hole interaction is not included, with the first prominent peak locating at the energy gap predicted by *GW* calculations. Dramatic changes occur upon the inclusion of the electron−hole interaction. All spectra shift toward lower energies, and the intensities of peaks are significantly suppressed. However, similar profiles are still noticeable for all spectra, with new prominent peaks emerging below the onset of the spectra without electron−hole interaction. Further analysis into these peaks reveals that they are contributed by a pair of 2-fold degenerate excitons which originate from the transitions between the degenerate frontier orbitals (more details in section II of the Supporting Information). One of this pair of excitons is bright only if the polarization of the incident light is along the *x* direction, as indicated in Figure 1, while the other one becomes bright when the polarization is along the *y* direction. Thus, they are labeled as "E_x" and "E_y", respectively. The degeneracy of this pair of exciton is attributed to the rotation symmetry of hexagonal geometry. The existence of

paired bright degenerate excitons is also predicted in triangular GQDs.[54] The exciton binding energies, defined as the energy difference between excitation energy and HOMO−LUMO energy gap at the *GW* level, are listed in Table 1. The exciton binding energies for AM-13 and ZZ-37 are 1.98 and 1.24 eV, respectively, much larger than that of 1.10 eV for 9-AGNR and 0.89 eV for 15-AGNR.[69] Such large exciton binding energies are attributed to the quantum confinement and reduced screening due to reduced dimensionality. Quantum confinement results in larger overlap of the electron and the hole. Meanwhile, the screening is reduced due to the larger energy gap. These effects lead to stronger interaction between the electron and the hole and result in larger binding energies.[45] Similar to the case of energy gap, the exciton binding energy decreases as the lateral size increases. Also, the exciton binding energy for AM-43 is larger than that of ZZ-37 (1.37−1.24 eV), in spite of a larger size (2.05−1.84 nm). This anomaly stems from the larger energy gap of AM-43. The binding energy for AM-43 is larger than that of 0.25 eV,[53] predicted for triangular GQD with smaller size, probably arising from the different geometry. For all these GQDs, dark excitons are observed below the degenerate bright ones. The dark nature of lower excitons and the 2-fold degeneracy of the bright excitons are consistent with TDDFT results.[32] Specially, for GQD AM-43 TDDFT calculations predict the energies of the two lowest dark excitons to be 1.90 and 1.97 eV,[32] respectively, in good agreement with the current results of 1.88 and 1.98 eV.

To further investigate the spatial correlation of the electron and the hole, the radial distribution of exciton E_x in real-space is depicted in Figure 4a−f. The projected electron density $|\Phi(r_e)|^2$ = $\int_0^\pi d\theta_e \int_0^{2\pi} d\varphi_e \ |\Phi(r_e, \theta_e, \varphi_e, \vec{x}_h)|^2$ with the hole fixed at the geometry center is plotted along the radius of GQD after integrating out the polar angle θ and azimuthal angle φ in a spherical coordinate system centered at the hole. The radial distribution suggests that the extent of exciton E_x gets larger as the lateral size increases for armchair-edged GQDs. The extent for ZZ-19 is almost of the same size as ZZ-07 except redistribution of the local maxima, while that of ZZ-37 is the largest. The radii of E_x, defined as $\bar{r}_e = \int_0^{+\infty} r_e' \cdot |\Phi(r_e')|^2 dr_e'$, are listed in Table 1. As indicated, the radius increases monotonically as the lateral size increases for both armchair and zigzag edged GQDs, which is in good consistency with the relation between exciton binding energy and lateral size. For exciton, with a smaller radius, the electron and the hole are confined within a narrower area, leading to stronger interaction and eventually larger exciton binding energy. It is worth attention that the edge geometry is also of great importance in determining binding energy, as mentioned above, since the exciton binding energy for AM-43 is larger than that for ZZ-37, in spite of a larger exciton radius.

Apart from singlet excited states, the luminescence may also be influenced by low-lying triplet states through their mixing with a small amount of singlet via spin−orbit coupling, leading to long luminescence lifetime. The singlet−triplet splitting for E_x is in the range of 0.62−1.63 eV, much larger than that of other carbon allotropes, as 0.15 and 0.07 eV are predicted for 9-AGNR and 15-AGNR whose widths are comparable to AM-13 and ZZ-37, respectively.[69] Such large splitting may reduce the probability of nonradiative transition from singlet to triplet state and result in high fluorescence luminescent yield.[72] The large splitting is attributed to the strong electron−hole overlap,
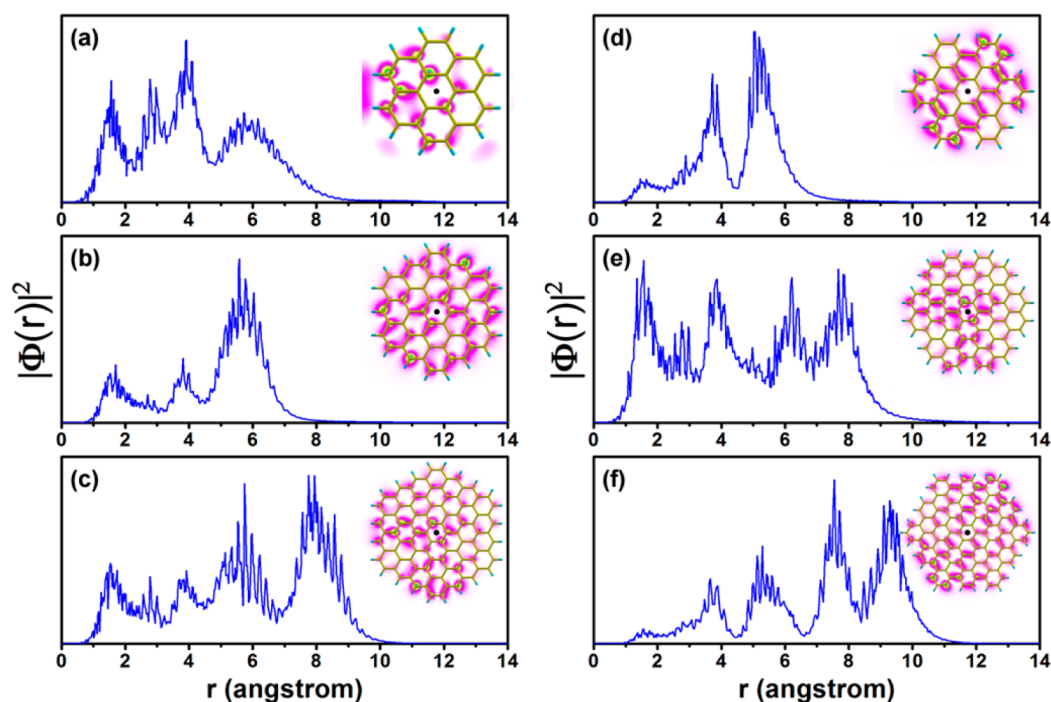
Figure 4. (a−f) Radial electron distribution of exciton E_x for ZZ-07, ZZ-09, ZZ-37, AM-13, AM-31, and AM-43, respectively. Plotted quantity is electron amplitude square with the hole fixed at the geometry center of GQD, as indicated by black dots in insets. Integration over the polar angle θ and the azimuthal angle φ has been performed in a spherical coordinate system centered at the position of the hole. The inset in each figure demonstrates the electron distribution of exciton E_x after integrating out the z coordinate perpendicular to the plane on which the GQD is placed. The magenta areas denote low electron density areas, while the yellow areas denote high ones.

which enhances the repulsive exchange interaction K^x in turn. The electron−hole overlap can be measured approximately by the average of wave function overlap between the occupied and unoccupied frontier orbitals involved in the optical transitions of E_x. For one pair of occupied and unoccupied orbitals, the wave function overlap is defined as $O[\psi_o, \psi_u] = \int |\psi_o(\vec{r})| \cdot |\psi_u(\vec{r})| dV$, where ψ_o and ψ_u denote the occupied and unoccupied orbitals, respectively. The electron−hole overlaps of GQDs are summarized in Table 1. Clearly, the splitting decreases monotonically with the decrease of the overlap for zigzag-edged GQDs. The same trend is also observed for armchair-edged ones, with the only exception of AM-31. In fact, the overlap in AM-31 is very close to that in zigzag-edged ones. Also, the corners of AM-31 are more "zigzag-like" than that of AM-13 and AM-43, as depicted in Figure 1. Thus, the anomaly for AM-31 in the relation between singlet−triplet splitting and electron−hole overlap can be attributed to the influence of the corner geometry of GQDs.

IV. CONCLUSION

In summary, the electronic structure and optical properties of GQDs have been investigated via the $GW + BSE$ approach. Many-body effects are found to be significant in these low dimensional materials: the quasi-particle corrections to band gap can be several eV; the absorption spectra shift toward low energies when electron−hole interaction is included, with new peaks emerging below the onset of the spectra without electron−hole interaction, which correspond to a series of bright bound excitons; the lowest bright bound excitons have binding energies larger than 1 eV; the quasi-particle corrections and exciton binding energies are much larger than those of other carbon allotropes with higher dimensionality like

nanotubes and nanoribbons. Such large many-body effects stem from the quantum confinement and the reduced screening due to lower dimensionality. The results also reveal the importance of the lateral size and the edge geometry in determining the band gap and exciton binding energy of GQDs. Both band gap and binding energy of the first bright exciton decrease as the lateral size of GQD increases; however, the band gap and exciton binding energy of AM-43 are larger than those of ZZ-37 in spite of a larger lateral size of AM-43. The lowest bright excitons that contribute to the first absorption peak originate from transitions between degenerate frontier orbitals, and are 2-fold degenerate. Moreover, dark excitons are also observed below the lowest bright ones. The spin singlet−triplet splitting is larger than that of other carbon allotropes with higher dimensionality due to the large electron−hole overlap, which may reduce the probability of nonradiative transition from singlet to triplet state and result in high fluorescence luminescent yield. The degeneracy and large binding energy of the bright exciton, the dark nature of the lowest exciton and the large spin singlet−triplet splitting indicate that GQDs are of promising application potential in optoelectronics like luminescent devices and photovoltaics.

■ ASSOCIATED CONTENT

ⓢ Supporting Information

Spatial distribution of summated charge density of degenerate frontier orbitals (SI-I); Detailed analysis of the transitions of the bright excitons corresponding to the first peak in the absorption spectrum (SI-II). This material is available free of charge via the Internet at http://pubs.acs.org.

AUTHOR INFORMATION

Corresponding Author

*E-mail: jlwang@seu.edu.cn. Phone: +86-25-52090600-8304.

Notes

The authors declare no competing financial interest.

ACKNOWLEDGMENTS

REFERENCES

(1) Novoselov, K. S.; Geim, A. K.; Morozov, S. V.; Jiang, D.; Zhang, Y.; Dubonos, S. V.; Grigorieva, I. V.; Firsov, A. A. Electric Field Effect in Atomically Thin Carbon Films. *Science* **2004**, *306*, 666−669.

(2) Katsnelson, M. I.; Novoselov, K. S.; Geim, A. K. Chiral Tunnelling and the Klein Paradox in Graphene. *Nat. Phys.* **2006**, *2*, 620−625.

(3) Bolotin, K. I.; Sikes, K. J.; Jiang, Z.; Klima, M.; Fudenberg, G.; Hone, J.; Kim, P.; Stormer, H. L. Ultrahigh Electron Mobility in Suspended Graphene. *Solid State Commun.* **2008**, *146*, 351−355.

(4) Balandin, A. A.; Ghosh, S.; Bao, W.; Calizo, I.; Teweldebrhan, D.; Miao, F.; Lau, C. N. Superior Thermal Conductivity of Single-Layer Graphene. *Nano Lett.* **2008**, *8*, 902−907.

(5) Lee, C.; Wei, X.; Kysar, J. W.; Hone, J. Measurement of the Elastic Properties and Intrinsic Strength of Monolayer Graphene. *Science* **2008**, *321*, 385−388.

(6) Nair, R. R.; Blake, P.; Grigorenko, A. N.; Novoselov, K. S.; Booth, T. J.; Stauber, T.; Peres, N. M. R.; Geim, A. K. Fine Structure Constant Defines Visual Transparency of Graphene. *Science* **2008**, *320*, 1308.

(7) Singh, V.; Joung, D.; Zhai, L.; Das, S.; Khondaker, S. I.; Seal, S. Graphene Based Materials: Past, Present and Future. *Prog. Mater. Sci.* **2011**, *56*, 1178−1271.

(8) Schedin, F.; Geim, A. K.; Morozov, S. V.; Hill, E. W.; Blake, P.; Katsnelson, M. I.; Novoselov, K. S. Detection of Individual Gas Molecules Adsorbed on Graphene. *Nat. Mater.* **2007**, *6*, 652−655.

(9) Avouris, P.; Chen, Z.; Perebeinos, V. Carbon-Based Electronics. *Nat. Nanotechnol.* **2007**, *2*, 605−615.

(10) Elias, D. C.; Nair, R. R.; Mohiuddin, T. M. G.; Morozov, S. V.; Blake, P.; Halsall, M. P.; Ferrari, A. C.; Boukhvalov, D. W.; Katsnelson, M. I.; Geim, A. K.; et al. Control of Graphene's Properties by Reversible Hydrogenation: Evidence for Graphane. *Science* **2009**, *323*, 610−613.

(11) Ma, L.; Wang, J.; Ding, F. Strain-Induced Orientation-Selective Cutting of Graphene into Graphene Nanoribbons on Oxidation. *Angew. Chem., Int. Ed.* **2012**, *51*, 1161−1164.

(12) Wang, J.; Ma, L.; Yuan, Q.; Zhu, L.; Ding, F. Transition-Metal-Catalyzed Unzipping of Single-Walled Carbon Nanotubes into Narrow Graphene Nanoribbons at Low Temperature. *Angew. Chem., Int. Ed.* **2011**, *50*, 8041−8045.

(13) Yan, X.; Cui, X.; Li, B.; Li, L. Large, Solution-Processable Graphene Quantum Dots as Light Absorbers for Photovoltaics. *Nano Lett.* **2010**, *10*, 1869−1873.

(14) Neubeck, S.; Ponomarenko, L. A.; Freitag, F.; Giesbers, A. J. M.; Zeitler, U.; Morozov, S. V.; Blake, P.; Geim, A. K.; Novoselov, K. S. From One Electron to One Hole: Quasiparticle Counting in Graphene Quantum Dots Determined by Electrochemical and Plasma Etching. *Small* **2010**, *6*, 1469−1473.

(15) Li, L.; Yan, X. Colloidal Graphene Quantum Dots. *J. Phys. Chem. Lett.* **2010**, *1*, 2572−2576.

(16) Li, M.; Wu, W.; Ren, W.; Cheng, H.-M.; Tang, N.; Zhong, W.; Du, Y. Synthesis and Upconversion Luminescence of N-Doped Graphene Quantum Dots. *Appl. Phys. Lett.* **2012**, *101*, 103107.

(17) Liu, R.; Wu, D.; Feng, X.; Müllen, K. Bottom-Up Fabrication of Photoluminescent Graphene Quantum Dots with Uniform Morphology. *J. Am. Chem. Soc.* **2011**, *133*, 15221−15223.

(18) Kim, S.; Hwang, S. W.; Kim, M.-K.; Shin, D. Y.; Shin, D. H.; Kim, C. O.; Yang, S. B.; Park, J. H.; Hwang, E.; Choi, S.-H.; et al. Anomalous Behaviors of Visible Luminescence from Graphene Quantum Dots: Interplay between Size and Shape. *ACS Nano* **2012**, *6*, 8203−8208.

(19) Mueller, M. L.; Yan, X.; McGuire, J. A.; Li, L. Triplet States and Electronic Relaxation in Photoexcited Graphene Quantum Dots. *Nano Lett.* **2010**, *10*, 2679−2682.

(20) Jing, Y.; Zhu, Y.; Yang, X.; Shen, J.; Li, C. Ultrasound-Triggered Smart Drug Release from Multifunctional Core−Shell Capsules One-Step Fabricated by Coaxial Electrospray Method. *Langmuir* **2010**, *27*, 1175−1180.

(21) Sun, X.; Liu, Z.; Welsher, K.; Robinson, J.; Goodwin, A.; Zaric, S.; Dai, H. Nano-Graphene Oxide for Cellular Imaging and Drug Delivery. *Nano Lett.* **2008**, *1*, 203−212.

(22) Zhu, S.; Zhang, J.; Qiao, C.; Tang, S.; Li, Y.; Yuan, W.; Li, B.; Tian, L.; Liu, F.; Hu, R.; et al. Strongly Green-Photoluminescent Graphene Quantum Dots for Bioimaging Applications. *Chem. Commun.* **2011**, *47*, 6858−6860.

(23) Zhao, J.; Chen, G.; Zhu, L.; Li, G. Graphene Quantum Dots-Based Platform for the Fabrication of Electrochemical Biosensors. *Electrochem. Commun.* **2011**, *13*, 31−33.

(24) Li, Y.; Zhao, Y.; Cheng, H.; Hu, Y.; Shi, G.; Dai, L.; Qu, L. Nitrogen-Doped Graphene Quantum Dots with Oxygen-Rich Functional Groups. *J. Am. Chem. Soc.* **2011**, *134*, 15−18.

(25) Li, Y.; Hu, Y.; Zhao, Y.; Shi, G.; Deng, L.; Hou, Y.; Qu, L. An Electrochemical Avenue to Green-Luminescent Graphene Quantum Dots as Potential Electron-Acceptors for Photovoltaics. *Adv. Mater.* **2011**, *23*, 776−780.

(26) Yan, X.; Li, B.; Cui, X.; Wei, Q.; Tajima, K.; Li, L. Independent Tuning of the Band Gap and Redox Potential of Graphene Quantum Dots. *J. Phys. Chem. Lett.* **2011**, *2*, 1119−1124.

(27) Pan, D.; Zhang, J.; Li, Z.; Wu, M. Hydrothermal Route for Cutting Graphene Sheets into Blue-Luminescent Graphene Quantum Dots. *Adv. Mater.* **2010**, *22*, 734−738.

(28) Jin, S. H.; Kim, D. H.; Jun, G. H.; Hong, S. H.; Jeon, S. Tuning the Photoluminescence of Graphene Quantum Dots through the Charge Transfer Effect of Functional Groups. *ACS Nano* **2012**, *7*, 1239−1245.

(29) Shi, H.; Barnard, A. S.; Snook, I. K. Quantum Mechanical Properties of Graphene Nano-Flakes and Quantum Dots. *Nanoscale* **2012**, *4*, 6761−6767.

(30) Ma, W.-L.; Li, S.-S. Electrically Controllable Energy Gaps in Graphene Quantum Dots. *Appl. Phys. Lett.* **2012**, *100*, 163109.

(31) Chen, R. B.; Chang, C. P.; Lin, M. F. Electric-Field-Tunable Electronic Properties of Graphene Quantum Dots. *Phys. E (Amsterdam, Neth.)* **2010**, *42*, 2812−2815.

(32) Schumacher, S. Photophysics of Graphene Quantum Dots: Insights from Electronic Structure Calculations. *Phys. Rev. B* **2011**, *83*, 081417.

(33) Rohlfing, M.; Louie, S. G. Optical Excitations in Conjugated Polymers. *Phys. Rev. Lett.* **1999**, *82*, 1959−1962.

(34) Ruini, A.; Caldas, M. J.; Bussi, G.; Molinari, E. Solid State Effects on Exciton States and Optical Properties of PPV. *Phys. Rev. Lett.* **2002**, *88*, 206403.

(35) Spataru, C. D.; Ismail-Beigi, S.; Benedict, L. X.; Louie, S. G. Excitonic Effects and Optical Spectra of Single-Walled Carbon Nanotubes. *Phys. Rev. Lett.* **2004**, *92*, 077402.

(36) Chang, E.; Bussi, G.; Ruini, A.; Molinari, E. Excitons in Carbon Nanotubes: An Ab Initio Symmetry-Based Approach. *Phys. Rev. Lett.* **2004**, *92*, 196401.

(37) Yang, L.; Spataru, C. D.; Louie, S. G.; Chou, M. Y. Enhanced Electron-Hole Interaction and Optical Absorption in a Silicon Nanowire. *Phys. Rev. B* **2007**, *75*, 201304.

(38) Spataru, C. D.; Ismail-Beigi, S.; Benedict, L. X.; Louie, S. G. Quasiparticle Energies, Excitonic Effects and Optical Absorption

Spectra of Small-Diameter Single-Walled Carbon Nanotubes. *Appl. Phys. A: Mater. Sci. Process.* **2004**, *78*, 1129−1136.

(39) Spataru, C. D.; Ismail-Beigi, S.; Capaz, R. B.; Louie, S. G. Theory and Ab Initio Calculation of Radiative Lifetime of Excitons in Semiconducting Carbon Nanotubes. *Phys. Rev. Lett.* **2005**, *95*, 247402.

(40) Deslippe, J.; Spataru, C. D.; Prendergast, D.; Louie, S. G. Bound Excitons in Metallic Single-Walled Carbon Nanotubes. *Nano Lett.* **2007**, *7*, 1626−1630.

(41) Prezzi, D.; Varsano, D.; Ruini, A.; Marini, A.; Molinari, E. Optical Properties of Graphene Nanoribbons: The Role of Many-Body Effects. *Phys. Rev. B* **2008**, *77*, 041404.

(42) Yang, L.; Cohen, M. L.; Louie, S. G. Excitonic Effects in the Optical Spectra of Graphene Nanoribbons. *Nano Lett.* **2007**, *7*, 3112−3115.

(43) Yang, L.; Cohen, M. L.; Louie, S. G. Magnetic Edge-State Excitons in Zigzag Graphene Nanoribbons. *Phys. Rev. Lett.* **2008**, *101*, 186401.

(44) Zhu, X.; Su, H. Excitons of Edge and Surface Functionalized Graphene Nanoribbons. *J. Phys. Chem. C* **2010**, *114*, 17257−17262.

(45) Wirtz, L.; Marini, A.; Rubio, A. Excitons in Boron Nitride Nanotubes: Dimensionality Effects. *Phys. Rev. Lett.* **2006**, *96*, 126104.

(46) Park, C.-H.; Spataru, C. D.; Louie, S. G. Excitons and Many-Electron Effects in the Optical Response of Single-Walled Boron Nitride Nanotubes. *Phys. Rev. Lett.* **2006**, *96*, 126105.

(47) Wang, S.; Chen, Q.; Wang, J. Optical Properties of Boron Nitride Nanoribbons: Excitonic Effects. *Appl. Phys. Lett.* **2011**, *99*, 063114.

(48) Yang, L.; Deslippe, J.; Park, C.-H.; Cohen, M. L.; Louie, S. G. Excitonic Effects on the Optical Response of Graphene and Bilayer Graphene. *Phys. Rev. Lett.* **2009**, *103*, 186802.

(49) Trevisanutto, P. E.; Holzmann, M.; Côté, M.; Olevano, V. Ab Initio High-Energy Excitonic Effects in Graphite and Graphene. *Phys. Rev. B* **2010**, *81*, 121405.

(50) Park, C.-H.; Louie, S. G. Tunable Excitons in Biased Bilayer Graphene. *Nano Lett.* **2010**, *10*, 426−431.

(51) Yang, L. Excitons in Intrinsic and Bilayer Graphene. *Phys. Rev. B* **2011**, *83*, 085405.

(52) Arnaud, B.; Lebègue, S.; Rabiller, P.; Alouani, M. Huge Excitonic Effects in Layered Hexagonal Boron Nitride. *Phys. Rev. Lett.* **2006**, *96*, 026402.

(53) Güçlü, A. D.; Potasz, P.; Hawrylak, P. Excitonic Absorption in Gate-Controlled Graphene Quantum Dots. *Phys. Rev. B* **2010**, *82*, 155445.

(54) Ozfidan, I.; Korkusinski, M.; Güçlü, A. D.; McGuire, J. A.; Hawrylak, P. Microscopic Theory of the Optical Properties of Colloidal Graphene Quantum Dots. *Phys. Rev. B* **2014**, *89*, 085310.

(55) Perdew, J. P.; Zunger, A. Self-Interaction Correction to Density-Functional Approximations for Many-Electron Systems. *Phys. Rev. B* **1981**, *23*, 5048−5079.

(56) Rohlfing, M.; Louie, S. G. Electron-Hole Excitations and Optical Spectra from First Principles. *Phys. Rev. B* **2000**, *62*, 4927−4944.

(57) Hybertsen, M. S.; Louie, S. G. Electron Correlation in Semiconductors and Insulators: Band Gaps and Quasiparticle Energies. *Phys. Rev. B* **1986**, *34*, 5390−5413.

(58) Strinati, G. Dynamical Shift and Broadening of Core Excitons in Semiconductors. *Phys. Rev. Lett.* **1982**, *49*, 1519−1522.

(59) Strinati, G. Effects of Dynamical Screening on Resonances at Inner-Shell Thresholds in Semiconductors. *Phys. Rev. B* **1984**, *29*, 5718−5726.

(60) Bruneval, F.; Marques, M. A. L. Benchmarking the Starting Points of the GW Approximation for Molecules. *J. Chem. Theory Comput.* **2012**, *9*, 324−329.

(61) Perdew, J. P.; Wang, Y. Accurate and Simple Analytic Representation of the Electron-Gas Correlation Energy. *Phys. Rev. B* **1992**, *45*, 13244−13249.

(62) Perdew, J. P.; Burke, K.; Ernzerhof, M. Generalized Gradient Approximation Made Simple. *Phys. Rev. Lett.* **1996**, *77*, 3865−3868.

(63) Becke, A. D. Density-Functional Exchange-Energy Approximation with Correct Asymptotic Behavior. *Phys. Rev. A* **1988**, *38*, 3098−3100.

(64) Lee, C.; Yang, W.; Parr, R. G. Development of the Colle-Salvetti Correlation-Energy Formula into a Functional of the Electron Density. *Phys. Rev. B* **1988**, *37*, 785−789.

(65) Morov, S. L.; Carmichael, I.; Hug, G. L. *Handbook of Photochemistry*; M. Dekker: New York, 1993.

(66) Giannozzi, P.; Baroni, S.; Bonini, N.; Calandra, M.; Car, R.; Cavazzoni, C.; Ceresoli, D.; Chiarotti, G. L.; Cococcioni, M.; Dabo, I.; et al. QUANTUM ESPRESSO: A Modular and Open-Source Software Project for Quantum Simulations of Materials. *J. Phys.: Condens. Matter* **2009**, *21*, 395502.

(67) Deslippe, J.; Samsonidze, G.; Strubbe, D. A.; Jain, M.; Cohen, M. L.; Louie, S. G. BerkeleyGW: A Massively Parallel Computer Package for the Calculation of the Quasiparticle and Optical Properties of Materials and Nanostructures. *Comput. Phys. Commun.* **2012**, *183*, 1269−1289.

(68) Zarenia, M.; Chaves, A.; Farias, G. A.; Peeters, F. M. Energy Levels of Triangular and Hexagonal Graphene Quantum Dots: A Comparative Study between the Tight-Binding and Dirac Equation Approach. *Phys. Rev. B* **2011**, *84*, 245403.

(69) Wang, S.; Wang, J. Quasiparticle Energies and Optical Excitations in Chevron-Type Graphene Nanoribbon. *J. Phys. Chem. C* **2012**, *116*, 10193−10197.

(70) Barnard, A. S.; Snook, I. K. Modelling the Role of Size, Edge Structure and Terminations on the Electronic Properties of Graphene Nano-Flakes. *Model. Simul. Mater. Sci. Eng.* **2011**, *19*, 054001.

(71) Zhang, Z. Z.; Chang, K.; Peeters, F. M. Tuning of Energy Levels and Optical Properties of Graphene Quantum Dots. *Phys. Rev. B* **2008**, *77*, 235411.

(72) Zener, C. Non-Adiabatic Crossing of Energy Levels. *Proc. R. Soc. London, Ser. A* **1932**, *137*, 696−702.